Mechanics of Materials 198 (2024) 105089

Contents lists available at ScienceDirect

Mechanics of Materials

journal homepage: www.elsevier.com/locate/mecmat

Editor invited article

# Multiphysics topology optimization of magnetic materials with continuous magnetization orientations

Zhi Zhao [a], Chao Wang [a], Xiaojia Shelly Zhang [a,b,c,*]

[a] Department of Civil and Environmental Engineering, University of Illinois at Urbana Champaign, 205 North Mathews Ave, Urbana, IL 61801, USA
[b] Department of Mechanical Science and Engineering, University of Illinois Urbana-Champaign, USA
[c] National Center of Supercomputing Applications, USA

ARTICLE INFO

*Keywords:*
Topology optimization
Magnetic soft materials
Continuous magnetization orientations
Direct ink writing
Additive manufacturing
Multiphysics

ABSTRACT

In recent years, magnetic-responsive soft materials with high remanent magnetization have received significant attention due to their capacity for untethered and rapid actuation under magnetic fields, with diverse applications spanning robotics, biomedicine, and vibration mitigation. Most designs of the magnetic soft materials rely on discrete remanent magnetization orientations, which could limit the actuation performance because of the restricted selection of magnetization orientations and potentially cause fabrication challenges due to the sharp changes in magnetization orientations at the interfaces that may induce strong repelling forces. To expand the programmability and improve the fabricability of the magnetic soft materials, we enable design capability with optimal continuous magnetization orientations. This paper proposes a multiphysics topology optimization framework that concurrently optimizes topologies and continuous remanent magnetization distributions in the magnetic soft materials and structures. Employing the proposed approach, we design and investigate problems of letter programming, actuators, and metamaterials with magnetic actuation under large deformations. We demonstrate that the proposed strategy enhances design flexibility, improves performance, eliminates sharp changes in magnetization orientations, and is capable of creating non-intuitive designs that can achieve multiple functionalities. Finally, we prototype our optimized design to highlight its potential to bridge design optimization and direct-ink-writing fabrication of magnetic materials with continuously varying magnetization orientations.

## 1. Introduction

In recent years, there has been an increasing interest in research focused on magnetic-responsive soft materials capable of untethered and rapid actuation when subjected to magnetic fields. These materials have been used in diverse applications in various domains, including robotics (Lum et al., 2016; Kim et al., 2019), biomedicine (Ceylan et al., 2019; Zhou et al., 2021), vibration mitigation (Li et al., 2014; Kang et al., 2020), and electronics (Rahmati et al., 2023a). This study focuses on hard-magnetic soft materials (Zhao et al., 2019; Lu et al., 2023) with high remanent magnetization, which are created by embedding high-coercivity magnetic particles, such as neodymium–iron–boron alloy, into a soft matrix. This type of magnetic soft materials has displayed significant promise, offering flexible programmability and enabling a range of functionalities, including programmable shape transformations (Zhao and Zhang, 2023; Wu et al., 2020), tunable buckling responses (Zhao et al., 2023; Chen et al., 2021), and magnetoelectricity (Rahmati et al., 2023a,b). Additionally, advanced manufacturing techniques, such as direct ink writing (Kim et al., 2018), have been employed to produce magnetic soft materials with complex geometries and heterogeneous remanent magnetization distributions.

In the context of designing magnetic soft materials, while several studies have successfully designed magnetic soft materials through topology optimization (Zhao and Zhang, 2022; Wang et al., 2023; Tian et al., 2022) and machine learning (Ma et al., 2022; Lloyd et al., 2020) approaches, most of these designs utilize discrete remanent magnetization orientations. This feature may encounter performance limitations because of the restricted magnetization orientation choices and fabricability challenges arising from sharp changes in remanent magnetization at interfaces.

In this study, as illustrated in Fig. 1(a) and (b), we propose a multiphysics topology optimization framework for designing magnetic

Invited Editor: Yihui Zhang.
* Corresponding author at: Department of Civil and Environmental Engineering, University of Illinois at Urbana Champaign, 205 North Mathews Ave, Urbana, IL 61801, USA.
*E-mail address:* zhangxs@illinois.edu (X.S. Zhang).

https://doi.org/10.1016/j.mechmat.2024.105089
Received 16 March 2024; Received in revised form 23 June 2024; Accepted 9 July 2024
Available online 18 July 2024

soft materials and structures with continuous remanent magnetization orientations. We highlight that the remanent magnetization vector at each location in the design can have a continuously-selected (arbitrary) orientation. For brevity, we sometimes use the term "magnetization" for "remanent magnetization" in the paper. Also, the magnetization orientation flows continuously and smoothly in the optimized designs. This framework is developed using a density-based topology optimization approach (Bendsoe and Sigmund, 2003) and can concurrently optimize both their geometry and a continuous distribution of remanent magnetization. As shown in Fig. 1(c), designs incorporating continuous magnetization present three significant advantages: (1) Improved actuation performance is attainable, thanks to an expanded design space facilitated by arbitrary magnetization orientations; (2) Unfavorable sharp changes in spatial magnetization orientation flow are avoided, reducing repelling forces and enhancing fabricability; (3) Optimized designs with continuous magnetization orientation are highly compatible with the recently developed magnetic direct-ink-writing fabrication technique (Kim et al., 2018).

In Fig. 2, we present an illustrative example with a cantilever setup whose magnetization is optimized to attain a 5/8 circular shape under an upward magnetic field, supporting the advantages outlined in points 1 and 2. The applied constitutive model is detailed in Appendix A. By employing the proposed continuous magnetization optimization approach for the cantilever example, we can achieve the best fitting performance compared to designs optimized with discrete magnetization (using the design approach developed in our previous work Zhao and Zhang, 2022). We note that in discrete magnetization optimization, designs incorporating a large number of candidate magnetization orientations can approach the performance achieved through continuous magnetization optimization. However, introducing more candidate magnetization orientations typically results in a rise in computational burden and optimization complexity.

We introduce a design parameterization scheme that systematically represents the continuous remanent magnetization distribution and the geometry of the soft matrix. Through the interpolation of Helmholtz free energy function, we then characterize the nonlinear response of a given design under the applied magnetic field. We illustrate the effectiveness of this framework through several types of examples. These include shape-programmed letters, functional magnetic actuators by optimizing both topology and continuous magnetization, and magneto-mechanical metamaterials capable of controllable lateral deformation under pure mechanical stimulus and combined mechanical and magnetic stimuli. To showcase the manufacturability of the acquired designs with continuous magnetization orientations, we utilize a direct-ink-writing method to fabricate magnetic actuator designs and present experimental demonstrations of their enabled functionality.

The remainder of this paper is organized as follows. Section 2 introduces design parameterization schemes that systematically represent the continuous remanent magnetization distribution and the geometry of the soft matrix as well as the topology optimization formulation. Section 3 presents several design examples, including magnetic actuators and metamaterials, to demonstrate the unique advantages enabled by the proposed formulation. Section 4 shows the fabrication of magnetic actuator designs and experimental demonstrations. Section 5 provides concluding remarks. Appendix A presents the applied magneto-mechanical constitutive model. Appendix B reviews the design parameterization scheme for discrete magnetization orientations to generate results for comparison. Appendix C complements the paper by investigating the impact of magnetized areas on their adjacent regions due to non-zero magnetic susceptibility.

## 2. Topology optimization framework

In this section, we introduce the proposed density-based topology optimization framework. We start by presenting the parameterization scheme for continuous magnetization orientations, followed by the parameterization for the geometry variable and the interpolation of the energy function. We then provide a detailed explanation of the optimization formulation. We utilize a simplified constitutive model defined by a Helmholtz free energy function (Zhao et al., 2019) to model magnetic soft materials under large deformation, as presented in Appendix A. The finite element method is used to solve the magneto-mechanical boundary value problem. It is worth noting that our topology optimization approach is general and can adapt to various magneto-mechanical models.

### 2.1. Parameterization of continuous magnetization orientations

The continuous magnetization orientations involve two key features: one is to allow a continuous (arbitrary) option for the element-wise magnetization orientation, and the other is to enable spatially continuous magnetization orientation flow. Additionally, maintaining a constant magnitude is usually preferable for fabrication. Therefore, we also aim to impose constraints to promote a constant magnetization magnitude in the optimized designs. In the following, we provide specific details for parametrization schemes to achieve the continuous magnetization orientations.

#### 2.1.1. Continuous option of element-wise magnetization orientation

The two-dimensional (2D) element-wise residual magnetic flux density $\mathbf{B}_{\mathrm{r},e}$ (remanent magnetization $\mathbf{M}_{\mathrm{r},e} = \mathbf{B}_{\mathrm{r},e}/\mu_0$ where $\mu_0$ is the air permeability) in element $e$ of the design can be interpolated by two orthogonal and equal-magnitude residual magnetic flux density base vectors, denoted as $\mathbf{B}_{\mathrm{r}}^{(1)}$ and $\mathbf{B}_{\mathrm{r}}^{(2)}$. The residual magnetic flux density is expressed as:

$$\mathbf{B}_{\mathrm{r},e} = \overline{m}_e^{(1)}\mathbf{B}_{\mathrm{r}}^{(1)} + \overline{m}_e^{(2)}\mathbf{B}_{\mathrm{r}}^{(2)}. \tag{1}$$

By interpolating the base vectors by the physical magnetization variable $\overline{m}_e^{(1)}$ and $\overline{m}_e^{(2)}$, we can continuously select arbitrary orientation for the element-wise magnetization vector. Note that we use Cartesian representation for $\mathbf{B}_{\mathrm{r},e}$ instead of the polar representation to circumvent the associated local-minimal and $2\pi$ ambiguity issues (Nomura et al., 2015).

To constrain the upper bound of the magnetization magnitude, $(\overline{m}_e^{(1)})^2+(\overline{m}_e^{(2)})^2 \le 1$, we use an iso-parametric mapping scheme (Nomura et al., 2015), as illustrated in Fig. 3(a). The corresponding expression is provided by the following equation:

$$\begin{aligned} \overline{m}_e^{(1)} &= \textstyle\sum_{i=1}^{8} a_i^{(1)} N_i(\overline{\xi}_e^{(1)}, \overline{\xi}_e^{(2)}) \\ \overline{m}_e^{(2)} &= \textstyle\sum_{i=1}^{8} a_i^{(2)} N_i(\overline{\xi}_e^{(1)}, \overline{\xi}_e^{(2)}) \end{aligned}, \tag{2}$$

where $a_i = \{a_i^{(1)}, a_i^{(2)}\}^T, i = 1...8$ is the coordinate of the $i$th node on the mapped circular shape (as shown in Fig. 3a); $\overline{\xi}_e^{(1,2)}$ is the element-wise intermediate design variable with the range of $[-1, 1]$; the mapping function $N_i(\cdot)$, inspired by the eight-node biquadratic quadrilateral element, is given by

$$\begin{cases} N_1 = -(1-\overline{\xi}_e^{(1)})(1-\overline{\xi}_e^{(2)})(1+\overline{\xi}_e^{(1)}+\overline{\xi}_e^{(2)})/4 \\ N_2 = (1-\overline{\xi}_e^{(1)})(1-\overline{\xi}_e^{(2)})(1+\overline{\xi}_e^{(1)})/2 \\ N_3 = -(1+\overline{\xi}_e^{(1)})(1-\overline{\xi}_e^{(2)})(1-\overline{\xi}_e^{(1)}+\overline{\xi}_e^{(2)})/4 \\ N_4 = (1+\overline{\xi}_e^{(1)})(1-\overline{\xi}_e^{(2)})(1+\overline{\xi}_e^{(2)})/2 \\ N_5 = -(1+\overline{\xi}_e^{(1)})(1+\overline{\xi}_e^{(2)})(1-\overline{\xi}_e^{(1)}-\overline{\xi}_e^{(2)})/4 \\ N_6 = (1-\overline{\xi}_e^{(1)})(1+\overline{\xi}_e^{(2)})(1+\overline{\xi}_e^{(1)})/2 \\ N_7 = -(1+\overline{\xi}_e^{(1)})(1+\overline{\xi}_e^{(2)})(1+\overline{\xi}_e^{(1)}-\overline{\xi}_e^{(2)})/4 \\ N_8 = (1-\overline{\xi}_e^{(1)})(1-\overline{\xi}_e^{(2)})(1+\overline{\xi}_e^{(2)})/2 \end{cases}. \tag{3}$$

By employing the iso-parametric mapping, we can constrain the upper bound of the magnetization magnitude. To promote a magnetization distribution with constant magnitude, we also apply a lower-bound magnitude constraint incorporated in Formulation (7).

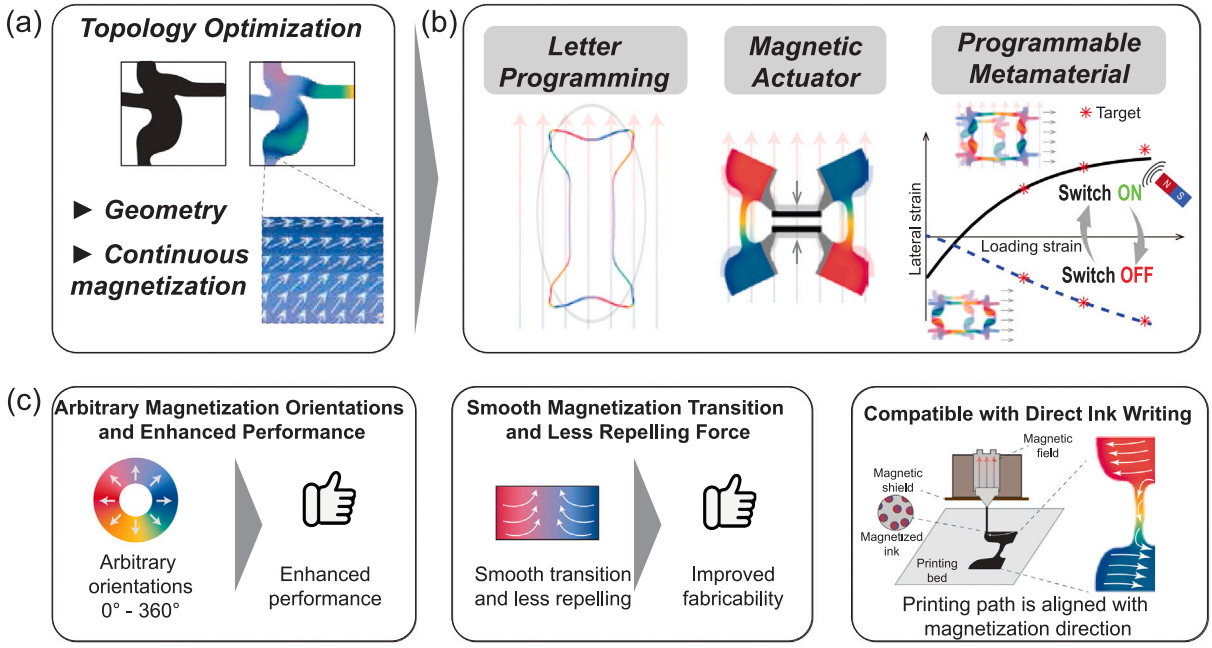


**Fig. 1.** Topology optimization for magnetic materials with continuous magnetization orientations: (a) design variables, (b) achievable functionalities, and (c) three notable advantages.

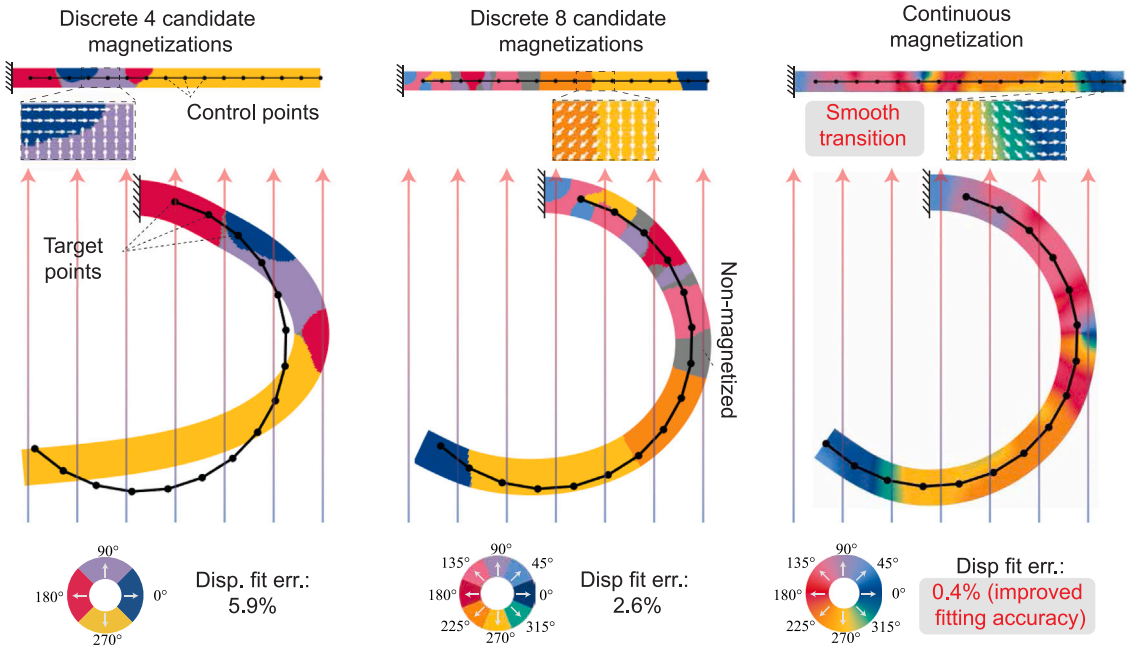


**Fig. 2.** Illustrative example: A cantilever with optimized magnetization orientations deforming to a 5/8 circular shape under a prescribed external magnetic field, highlighting improved performance (reduced fit error) and smooth magnetization transition compared to designs with discrete magnetization orientations.

### 2.1.2. Spatial continuity of magnetization orientation

To enable a spatial continuity of magnetization orientation, ensuring a smooth flow of the magnetization vector in the optimized designs, a filtering process is applied. We obtain the variables $\bar{\xi}_e^{(1,2)}$ through a distance-based filtering operation (Bourdin, 2001; Bendsoe and Sigmund, 2003). The expression is given by

$$\bar{\xi}_e^{(j)} = \frac{\sum_{i\in\mathcal{J}_e(R_m)} w_m^{(i,e)} v_i \xi_i^{(j)}}{\sum_{i\in\mathcal{J}_e(R_m)} w_m^{(i,e)} v_i}, \quad j = 1, 2, \tag{4}$$

where $\boldsymbol{\xi}^{(1,2)}$ are the design variables in the optimization, the set $\mathcal{J}_e(R_m)$ represents the $e$th element set within a region defined by a circle centered at the centroid of the $e$th element with a radius of $R_m$, $v_i$ is the volume of the $i$th element, and the weighting factor $w_m^{(i,e)}(R_m)$ is determined by the distance between the centroids of the $i$th and $e$th elements (denoted as $\mathbf{X}_i$ and $\mathbf{X}_e$, respectively), which is given by $w_m^{(i,e)} = 1 - (|\mathbf{X}_i - \mathbf{X}_e| / R_m)$. Fig. 3(b) illustrates the magnetization orientation before and after the filtering process. The comparison shows that filtering effectively smooths the spatial continuity of the orientation.

### 2.2. Parameterization of geometry

We utilize a density-based approach to associate the geometry to a physical design variable $\bar{\rho}_e$ for each element, where $\bar{\rho}_e$ indicates

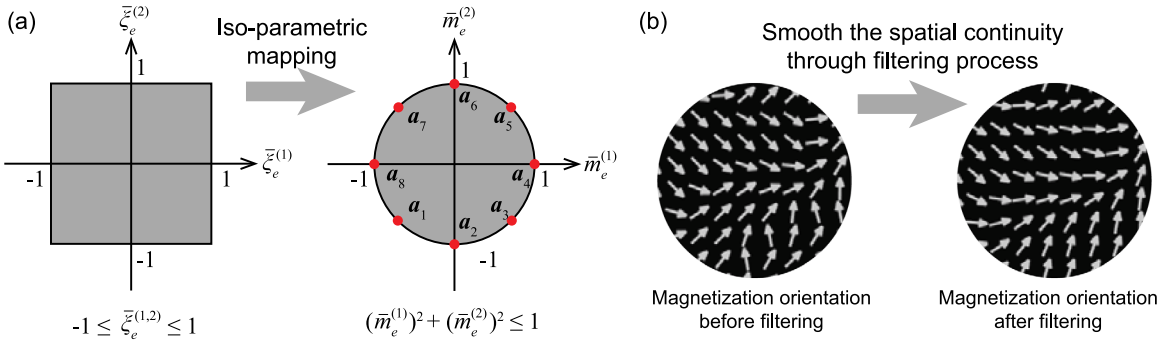


**Fig. 3.** Parameterization schemes for continuous magnetization vectors: (a) iso-parametric mapping; (b) filtering process.

whether a location in space is solid ($\overline{\rho}_e = 1$) or void ($\overline{\rho}_e = 0$). To ensure the discreteness of the design, the physical density variables $\overline{\rho}$ are obtained using a Heaviside projection operator with a threshold of 1/2 (Wang et al., 2011):

$$\overline{\rho}_e = \frac{\tanh(\frac{\beta_\rho}{2}) + \tanh(\beta_\rho(\widetilde{\rho}_e - \frac{1}{2}))}{2\tanh(\frac{\beta_\rho}{2})}, \tag{5}$$

where $\beta_\rho$ controls the discreteness of the projection. The symbol $\widetilde{\rho}_e$ represents the intermediate variable, which is obtained through a filtering process on the design variable $\rho_e$ using the distance-based filter Eq. (4) to address the checkerboard issue and control minimal member size (Bendsoe and Sigmund, 2003).

### 2.3. Interpolation of the Helmholtz free energy function

To characterize the nonlinear magneto-mechanical properties of magnetic soft materials, we apply an interpolation method to the Helmholtz free energy function based on physical variables $\overline{\rho}$ and $\overline{\mathbf{m}}^{(1,2)}$. The interpolated free energy $W_{\mathrm{I}}$ of element $e$ under load case $\ell$ is given by

$$W_{\mathrm{I}}\left(\overline{\rho}_e, \overline{m}_e^{(1)}, \overline{m}_e^{(2)}, \mathbf{u}_e^{(\ell)}\right) = \left(\epsilon + (1-\epsilon)\left(\overline{\rho}_e\right)^{p_\rho}\right) W_{\mathrm{E}}\left(\mathbf{u}_e^{(\ell)}\right) + \left(\overline{\rho}_e\right)^{p_\rho} W_{\mathrm{M}}\left(\mathbf{u}_e^{(\ell)}, \mathbf{B}_{\mathrm{r},e}(\overline{m}_e^{(1)}, \overline{m}_e^{(2)})\right), \tag{6}$$

where $\mathbf{u}_e^{(\ell)}$ is the displacement vector in element $e$ under the load case $\ell$, and we introduce a small value of $\epsilon = 10^{-5}$ to avoid numerical singularity. To penalize both hyperelastic stored energy and magnetic free energy and promote a nearly discrete design, we use the SIMP approach (Bendsøe, 1989; Bendsoe and Sigmund, 2003) (using power $p_\rho$) in the interpolation formula above, driving the variable $\overline{\rho}_e$ towards either 0 or 1. To alleviate excessive deformations of low-density regions that can lead to numerical instabilities during optimization, we employ an energy interpolation scheme (Wang et al., 2014a) for the hyperelastic stored energy $W_{\mathrm{E}}$.

### 2.4. Optimization formulation

Using the design space parameterization and free-energy interpolation schemes, we present a topology optimization formulation for generating magneto-actuated designs with continuous magnetization orientations. Formally, we formulate the topology optimization problem as follows:

$$\begin{aligned}
&\min_{\rho,\xi^{(1)},\xi^{(2)}} J\left(\mathbf{u}^{(\ell)}\right), \quad \ell \in 1,\dots,N_\ell \\
&\text{s.t.:} \quad \frac{\mathbf{v}^{\mathrm{T}}\overline{\rho}}{|\Omega_{\mathrm{h}}|} \le v_{\max}, \\
&\left\{\sum_{e=1}^{N_{\mathrm{e}}}\left[\frac{w_{\overline{\sigma}}(\overline{\rho}_e)}{v_e}\int_{\Omega_{\mathrm{h},e}} \overline{\sigma}_{\mathrm{VM}}\left(\overline{\sigma}_{\mathrm{E}}\left(\mathbf{u}^{(\ell)}\right)\right)\mathrm{d}\mathbf{X}\right]^{p_{\mathrm{n}}}\right\}^{1/p_{\mathrm{n}}} \le \overline{\sigma}_{\max}^{(\ell)}, \\
&\ell = 1,\dots,N_\ell, \\
&\frac{\sum_{e=1}^{N_{\mathrm{e}}}\left[\overline{\rho}_e\left(1-\left(1-\sqrt{(\overline{m}_e^{(1)})^2+(\overline{m}_e^{(2)})^2}\right)^{p_v}\right)\right]}{\sum_{e=1}^{N_{\mathrm{e}}}\overline{\rho}_e} \ge 1-\overline{\varepsilon}_v \\
&\mathbf{r}(\overline{\rho}, \overline{\mathbf{m}}^{(1)},\dots,\overline{\mathbf{m}}^{(N_{\mathrm{m}})}, \mathbf{u}^{(\ell)}) = \mathbf{0}, \quad \ell = 1,\dots,N_\ell, \\
&\mathbf{0} \le \rho \le \mathbf{1}, \\
&-\mathbf{1} \le \xi^{(1,2)} \le \mathbf{1},
\end{aligned} \tag{7}$$

where the converged displacement vector obtained under the load case $\ell$ is denoted by $\mathbf{u}^{(\ell)}$. The objective function evaluated at $\mathbf{u}^{(\ell)}$ is given by $J(\mathbf{u}^{(\ell)})$ whose expression depends on the specific application needs. The proposed optimization formulation includes a volume usage constraint, with $\mathbf{v}$ representing the element volume vector and $v_{\max}$ being the upper bound of the volume ratio assigned for matrix materials. Stress constraints (Duysinx and Bendsøe, 1998; Zhao and Zhang, 2022) are also incorporated to ensure that the maximum von Mises stress associated with the mechanical Cauchy stress tensor $\overline{\sigma}_{\mathrm{E}} = 1/J(\partial W_{\mathrm{E}}(\mathbf{F})/\partial\mathbf{F})\mathbf{F}^{\mathrm{T}}$ does not exceed a prescribed upper limit $\overline{\sigma}_{\max}^{(\ell)}$. To avoid singularity issues in stress-constrained topology optimization (Duysinx and Bendsøe, 1998; Bruggi, 2008), a relaxation approach is utilized. In this approach, a function $w_{\overline{\sigma}}(\overline{\rho}_e) \doteq \epsilon + (1-\epsilon)\overline{\rho}_e^{q_\rho}$ is defined, where $q_\rho < 1$. The maximum stress is estimated using the $p$-norm approach (Duysinx and Bendsøe, 1998) with the power of $p_{\mathrm{n}}$. It is worth noting that stress constraints serve as a numerical technique to prevent the optimized design from containing thin members and hinge-like connections and to limit the level of local deformations (Zhao and Zhang, 2022). To ensure $\sqrt{(\overline{m}_e^{(1)})^2+(\overline{m}_e^{(2)})^2}$ is close to 1, a magnetization lower-bound magnitude constraint (Nomura et al., 2015) is applied where $p_v \ge 1$ and $\overline{\varepsilon}_v$ is a small value to alleviate numerical issue. Additionally, the equilibriums solved by finite element analysis under each load case are nested constraints within the formulation.

We use a gradient-based update algorithm, specifically the method of moving asymptotes (Svanberg, 1987), to solve the proposed formulation (7). The sensitivities of objective and constraint functions with respect to the design variables are obtained through the adjoint method (Bendsoe and Sigmund, 2003; Wang et al., 2023).

## 3. Numerical examples

In this section, we present three numerical examples to illustrate the effectiveness of the proposed optimization framework in generating magneto-actuated designs with continuous magnetization orientations. Example 1 demonstrates the optimization of magnetizations with prescribed geometries for three shape-programmed letters. In Example 2, we obtain functional magnetic actuators by optimizing both topology and continuous magnetization. In Example 3, we create magneto-mechanical metamaterials capable of controllable lateral deformation under pure mechanical stimulus and combined mechanical and magnetic stimuli. Note that in Examples 1 and 3, we conduct comparisons with the designs featuring discrete magnetization orientations using the design method presented in Zhao and Zhang (2022) (refer to Appendix B for a brief review of the parameterization scheme for discrete magnetization orientations) to highlight the advantages of designs featuring continuous magnetization orientations.

### 3.1. Example 1: letter programming

In this example, our objective is to program magneto-actuated deformation to replicate the shapes of letters. As illustrated in Fig. 4(a), we have programmed the letters "UIUC" to be formed under upward magnetic fields by optimizing the magnetization distribution. The design domains, shown in Fig. 4(b), consist of in-plane elliptical stripes with an aspect ratio of 2 and a width of 0.5 mm. The out-of-plane thickness is 2 mm. The control and target points are indicated in black and red, respectively. To help each elliptical stripe achieve individual letter shapes, we customize the boundary conditions, control/target points, the magnitude of external magnetic fields, as well as the magnetization zone. We utilize material properties characterized from Ecoflex 00-30, incorporating magnetic particles at a volume ratio of 15% (see Appendix A for details). The magnitude of residual magnetic flux density is set at 100 mT, which is aligned with the magnetic characterization result for the same amount of magnetic particle inclusion (Zhao et al., 2023). In this example, our optimization focuses on the magnetization distribution to achieve target displacements at the control points. Since the geometry optimization is not incorporated, the volume and stress constraints are not applied in this example. The objective function is defined as follows:

$$J_1(\mathbf{u}) = \max_{\alpha\in\{1,\dots,N_\alpha\}} \sqrt{\left(u_\alpha - u_\alpha^*\right)^2}, \tag{8}$$

where $u_\alpha$ and $u_\alpha^*$ are the actual and target displacement at the $\alpha$th control degree of freedom (DOF), respectively; and $N_\alpha$ is the total number of control DOFs. The min–max objective is solved by bound formulation (Olhoff, 1989). To further evaluate the average fitting performance, we define a normalized error as follows:

$$\text{Disp. fit err.} = \frac{\sqrt{\sum_\alpha (u_\alpha - u_\alpha^*)^2}}{\sqrt{\sum_\alpha (u_\alpha^*)^2}}, \tag{9}$$

In Fig. 4(c), we present the results of optimized letter programming. We can observe that the UIUC shapes (three letters) are successfully achieved under upward magnetic fields, with a fitting error of less than 2.1%. In response to magnetic actuation, the optimized magnetizations exhibit a tendency to align with the direction of the applied magnetic fields, thereby inducing the deformation of the elliptical strips into the desired letter shapes. Upon closer inspection of the optimized magnetization distribution, we observe a seamless transition in magnetization directions enabled by the developed optimization framework. It should be acknowledged that the approach of programming letter shapes from closed elliptical shapes may have limitations when dealing with certain letters, particularly unsymmetrical ones like "G" and "R". However, by strategically setting up different initial shapes and boundary conditions, such as an open elliptical initial shape, we can perform the shape programming for these letters.

To further highlight the advantages of continuous magnetization distribution, we perform a comparative design optimization for the letter "I" using discrete magnetization parameterization and compare it with the continuous magnetization case in Fig. 5. In the discrete case, magnetization exhibits abrupt transitions, possibly leading to fabrication challenges due to stronger repelling forces. In contrast, the continuous magnetization design naturally resolves this issue. Additionally, the ability to choose arbitrary magnetization directions in the continuous case improves fitting accuracy by 9.1% compared to the discrete magnetization design.

### 3.2. Example 2: magnetic actuators

In this example, our objective is to create functional magnetic actuators, specifically designed for gripping and moving objects under applied magnetic fields. As shown in Fig. 6, the design domain has an in-plane size of 40 mm × 20 mm and an out-of-plane thickness of 5 mm, with both ends clamped. The central region of the domain is designated as the working area, tasked with gripping and moving objects. We set up nearly rigid components (black areas in the figure) for contact with objects, with two control points placed on the nearly rigid components. Linear springs are applied on these control points to model the reaction from the object. Within the working area, we prescribe the material as non-magnetized. We employ the material property characterized from polydimethylsiloxane (PDMS) with a base-to-agent ratio of 20 to 1 with magnetic particles at a volume ratio of 15% (see Appendix A for details). The magnitudes of external magnetic field and residual magnetic flux density are set at 50 mT and 100 mT, respectively. In this example, we set the volume fraction upper bound to be 0.3 and stress upper bound to be 0.1 MPa. The objective function is given by

$$J_2(\mathbf{u}^{(1)},\dots,\mathbf{u}^{(N_\ell)}) = \max_{\substack{\ell\in\{1,\dots,N_\ell\}\\ \alpha\in\{1,\dots,N_\alpha^{(\ell)}\}}} u_\alpha^{(\ell)}, \tag{10}$$

where $u_\alpha^{(\ell)}$ is the actual displacement at the $\alpha$th control DOF under the $\ell$th load condition; and $N_\alpha$ is the total number of control DOFs. The actual displacement $u_\alpha^{(\ell)}$ is defined to adopt the appropriate sign, ensuring that minimizing $u_\alpha^{(\ell)}$ is equivalent to maximizing it in the opposite direction, which aligns with the target direction. To evaluate the actuation performance, we define an average displacement $\overline{u}_{\text{out}}^{(\ell)}$ at the control points as:

$$\overline{u}_{\text{out}}^{(\ell)} = \frac{\sum_\alpha |u_\alpha^{(\ell)}|}{N_\alpha^{(\ell)}}, \quad \ell = 1,\dots,N_\ell. \tag{11}$$

In Fig. 7, we showcase the first type of optimized magnetic actuator design with two nearly rigid components moving inward for object gripping. We set the spring stiffness to be 0.25 N/m and the external magnetic field pointing upward. Both geometry and magnetization distributions are optimized simultaneously. The optimized structural shapes contain four bulky members (colored in red and blue) connected by slender and compliant members that act as hinges, allowing for large movements of the bulky members. These interconnected bulky members bend inward through magnetic torques, enabling the gripping action of the two nearly rigid components. We can observe that magnetization orientations in the design exhibit a smooth transition. This feature results in less repelling force and helps alleviate debonding issues, making it more favorable for fabrication.

In Fig. 8, we showcase the second type of optimized magnetic actuator design, capable of achieving dual functionalities. This actuator can grip objects under an upward magnetic field and move the object downward under a downward magnetic field. The spring stiffness is set to 0.125 N/m. A design challenge we face is the need for the upper nearly rigid component to move downward under opposite magnetic fields. Our topology optimization approach provides a solution to this challenging design problem by simultaneously optimizing geometry and continuous magnetization. The top part of the design features

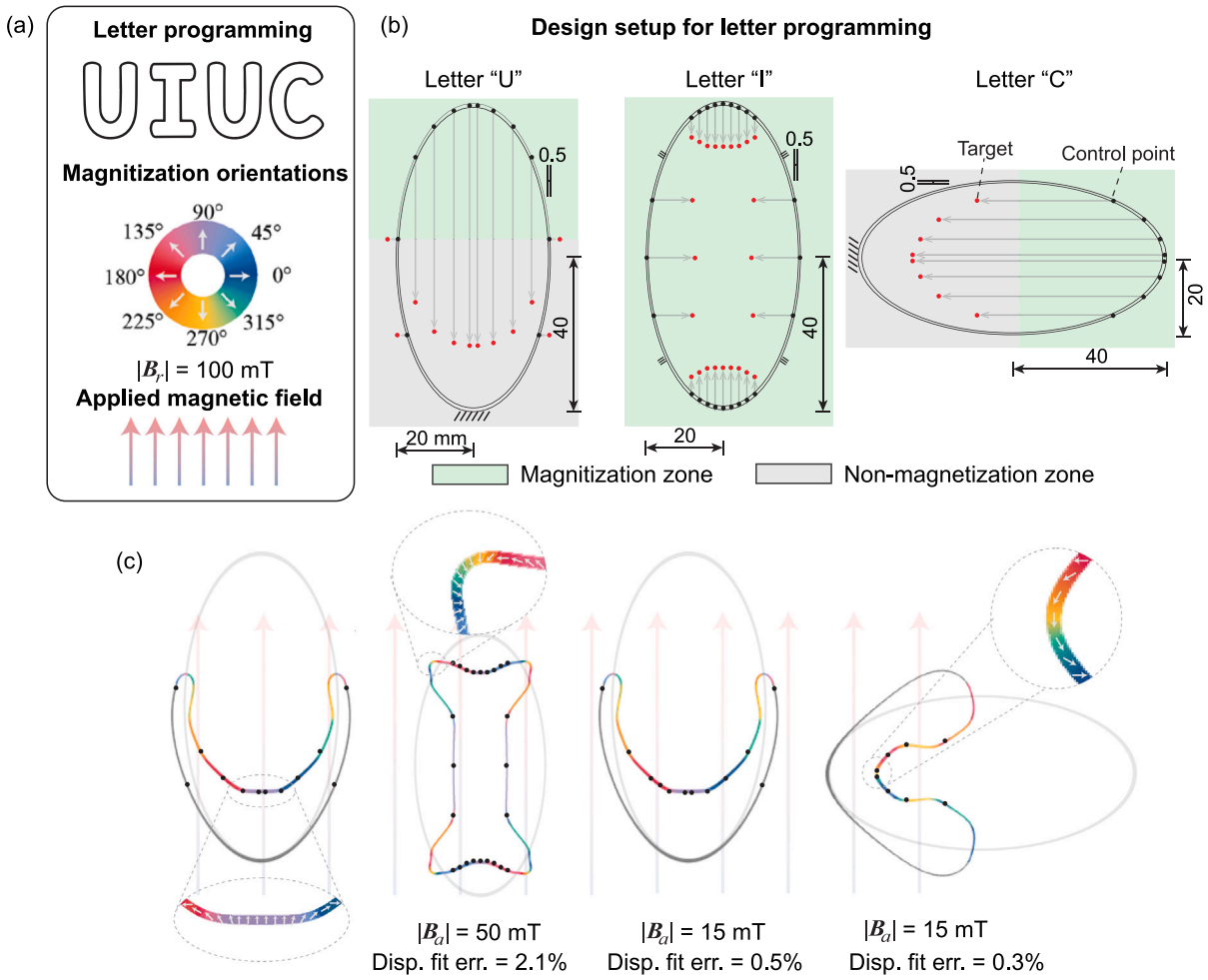


**Fig. 4.** Letter programming of magnetic responsive ellipse: (a) Letter programming of "UIUC", magnetization directions, and the direction of the applied magnetic field; (b) Design setup for the letter programming; (c) Optimized design and the deformed shapes.

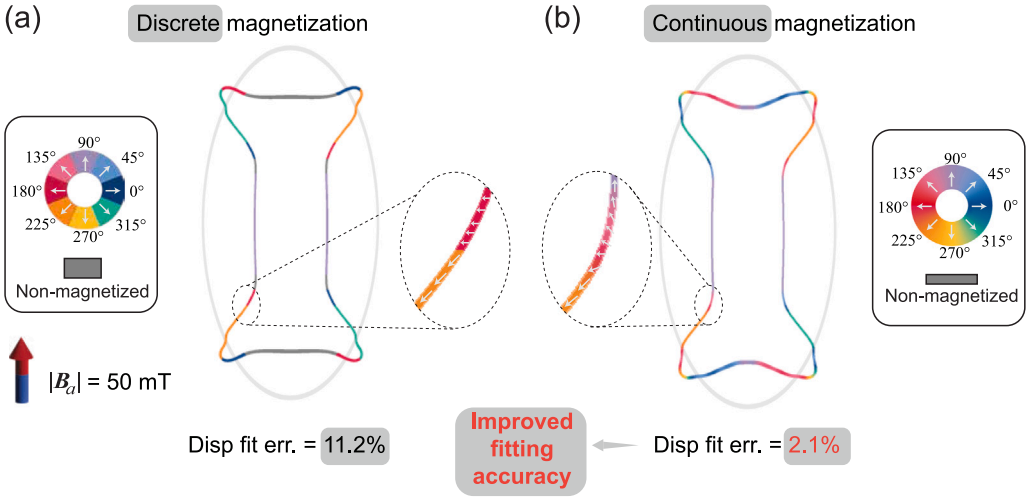


**Fig. 5.** Comparison of the letter programming based on the (a) discrete and (b) continuous magnetization.

two sets of bulky members connected by compliant small members, forming a non-intuitive compliant mechanism. The orange and green bulky members bend inward, driven by their optimized magnetization aligning with the upward external magnetic field. On the other hand, under the downward magnetic field, the light blue and light red members undergo inward bending due to the magnetic actuation. As a result, under both upward and downward magnetic fields, the upper nearly rigid component moves downward due to the inward bending of these two sets of bulky members. For the bottom part, where the target motion direction aligns with the corresponding magnetic field direction

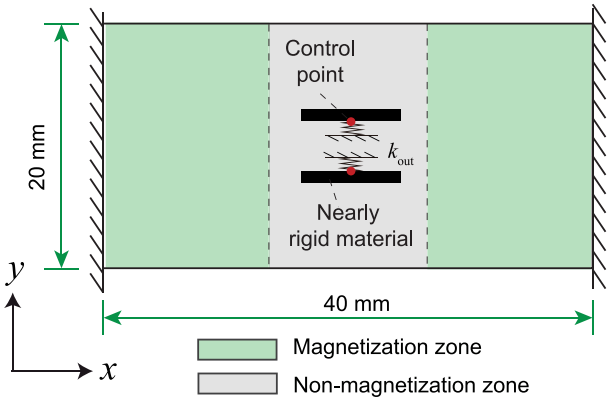


**Fig. 6.** Design setup of magnetic actuators.

in both cases, one set of magnetized members (in dark red and blue) is formed to achieve the desired actuation. The actuation displacements under both load cases are the same, $\overline{u}_{\text{out}}^{(1)} = \overline{u}_{\text{out}}^{(1)} = 1.08$ mm, due to the use of a min–max formulation. This design illustrates how topology optimization can facilitate intricate multi-functional designs that are not easily achieved through intuitions.

### 3.3. Example 3: programmable lateral deformation of magnetic metamaterial

In this example, we aim to program the lateral (perpendicular to the uniaxial loading direction) deformation of magnetic metamaterials under both purely mechanical and magneto-mechanical loads. As shown in Fig. 9(a), for a periodic metamaterial, effective material responses can be characterized using a unit cell. Consequently, we focus on designing a magneto-active unit cell. As shown in Fig. 9(b), within the square unit cell design domain with dimensions $L = 30$ mm and the out-of-plane thickness of $t = 5$ mm, we consider a scenario involving uniaxial tensile loading under periodic boundary conditions (Wang et al., 2014b). The left-bottom corner is fixed. The effective engineering strain is determined by the boundary displacement, derived through the average theorem (Nemat-Nasser and Hori, 2013), and is expressed as follows:

$$\begin{aligned} &\overline{\varepsilon}_{xx} = (u_{xx} - u_{xx0})/L, \quad \overline{\varepsilon}_{yx} = (u_{yx} - u_{yx0})/L, \\ &\overline{\varepsilon}_{xy} = (u_{xy} - u_{xy0})/L, \quad \overline{\varepsilon}_{yy} = (u_{yy} - u_{yy0})/L, \end{aligned} \tag{12}$$

where $u_{xx}$ and $u_{xx0}$ represent the displacement in the $x$ direction for node pairs located on the left and right boundaries. The definitions for the other displacement pairs remain consistent. It is important to note that, owing to the periodic boundary condition, the displacement pairs exhibit a uniform displacement difference. We apply a prescribed $\overline{\varepsilon}_{xx}$ to load the unit cell and program the lateral strain $\overline{\varepsilon}_{yy}$ under both purely mechanical and magneto-mechanical loads, respectively.

We utilize the material property characterized from Ecoflex 00-30 with embedded magnetic particles at a volume ratio of 15% (refer to Appendix A for details). The external magnetic field and residual magnetic flux density magnitudes are fixed at 50 mT and 100 mT, respectively. We note that, to ensure a smooth transition of magnetization orientations, the magnetization filtering (Eq. (4)) takes into account unit periodicity. For this example, we set the upper bounds for volume fraction and stress as 0.4 and 0.5 MPa, respectively. To program the lateral strain, we employ an error-minimization formulation. The objective function is defined as follows:

$$J_3(\mathbf{u}^{(1)}, \dots, \mathbf{u}^{(N_\ell)}) = \max_{\substack{\ell \in \{1,\dots,N_\ell\} \\ s \in \{1,\dots,N_s^{(\ell)}\}}} \sqrt{\left( \frac{\overline{\varepsilon}_{yy,s}^{(\ell)} - \overline{\varepsilon}_{yy,s}^{*(\ell)}}{\overline{\varepsilon}_{yy,s}^{*(\ell)}} \right)^2}, \tag{13}$$

with $\overline{\varepsilon}_{yy,s}^{*(\ell)}$ being the target lateral strain under the $\ell$th load case and $s$th load step ($N_s^{(\ell)}$ is the total load steps). Furthermore, to ensure connectivity in both $x$ and $y$ direction, we apply corresponding initial stiffness constraints (in addition to the constraints in Formulation (7)), stated as follows:

$$\overline{\sigma}_{xx} \geq \overline{\sigma}_{\min} \quad \text{and} \quad \overline{\sigma}_{yy} \geq \overline{\sigma}_{\min}, \tag{14}$$

where $\overline{\sigma}_{xx} = F_{xx}/(L \cdot t)$ and $\overline{\sigma}_{yy} = F_{yy}/(L \cdot t)$ represent the effective nominal stress in the $x$ and $y$ directions, resulting from a small mechanical load $\overline{\varepsilon}_{xx}$ and $\overline{\varepsilon}_{yy}$ (set at 0.06 in this example), respectively. The term $\overline{\sigma}_{\min}$ denotes the lower bound for effective stress (utilized as 1.3 kPa in this example). To quantify the error between the actual and target performance, we introduce a normalized error for the $\ell$th load case:

$$\text{Strain fit err.} = \frac{\sqrt{\sum_s (\overline{\varepsilon}_{yy,s}^{(\ell)} - \overline{\varepsilon}_{yy,s}^{*(\ell)})^2}}{\sqrt{\sum_s (\overline{\varepsilon}_{yy,s}^{*(\ell)})^2}}, \tag{15}$$

In Fig. 10, we present a design capable of achieving two levels of lateral contraction under purely mechanical and magneto-mechanical loads. The optimized design, as illustrated in Fig. 10(a), exhibits a seamless transition of magnetization orientations both within each unit cell and on the interfacial area of adjacent unit cells. Observing Fig. 10(b), it is evident that the actual lateral strain closely aligns with the targets, demonstrating an error of less than 2.7%. In the scenario of magneto-mechanical loading, the metamaterial experiences initial deformation when the strain $\overline{\varepsilon}_{xx}$ is zero. Throughout magneto-mechanical loading, it contracts more compared to the purely mechanical loading case, mainly due to the bending of the middle yellow members activated by the magnetic field. The magnetic field, acting as a switch, can alternate between the two programmed curves, enabling the metamaterial to achieve various levels of lateral contraction.

In Fig. 11, our objective is to obtain a more intricate lateral deformation, where the metamaterial undergoes lateral contraction under purely mechanical load and expansion under magneto-mechanical load. The optimized design is shown in Fig. 11(a). A complex and non-intuitive mechanism is discovered through the simultaneous optimization of geometry and continuous magnetization distribution. The optimized geometry features four cross-like members at the corners and two arch-like members in the center. When the design is mechanically stretched, the rotation of the cross shapes causes vertical compression in the arch-shaped members, leading to overall lateral contraction of the unit cell. Simultaneously optimizing continuous magnetization alongside the geometry alters the response to lateral expansion under magneto-mechanical load. The arch-shaped members vertically expand due to the alignment of magnetization with the external magnetic field, resulting in an overall lateral expansion.

To further showcase the advantage of the design with continuous magnetization orientation, we perform a comparative design optimization with discrete magnetization parameterization in Fig. 11(b). Compared to the design with discrete magnetization, the continuous magnetization design exhibits smooth transitions of magnetization orientations, which could help alleviate repelling forces and debonding issues. Their performance is presented in Fig. 11(c). We observe that the actual lateral strain of the continuous magnetization design aligns more closely with the target. For both mechanical and magneto-mechanical cases, the strain fitting errors (4.5% and 13.2%, respectively) for the continuous magnetization design are lower than those for the discrete magnetization design (7.8% and 21.6%, respectively). The enlarged design space gained from the arbitrary and continuous magnetization orientation option successfully reduces the fitting error by around 40%.

We also conduct a strain distribution analysis for the optimized design in Fig. 11(a) under purely mechanical stimulus and magneto-mechanical stimuli. We present the four components ($E_{xx}$, $E_{yx}$, $E_{xy}$, $E_{yy}$) of the Green–Lagrangian strain $E$ under the applied nominal strain of $\overline{\varepsilon}_{xx} = 0.5$ in Fig. 12. From the results, we can observe that overall

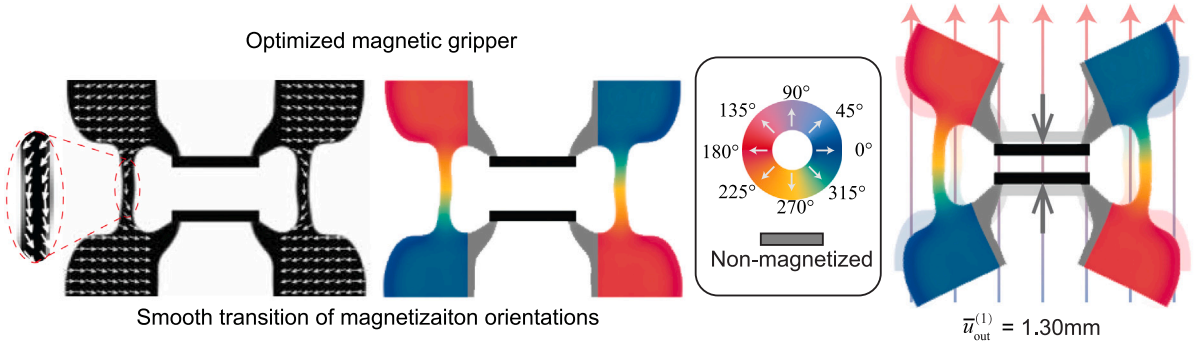


**Fig. 7.** Magnetic gripper with continuous magnetization orientations. (For interpretation of the references to colour in this figure legend, the reader is referred to the web version of this article.)

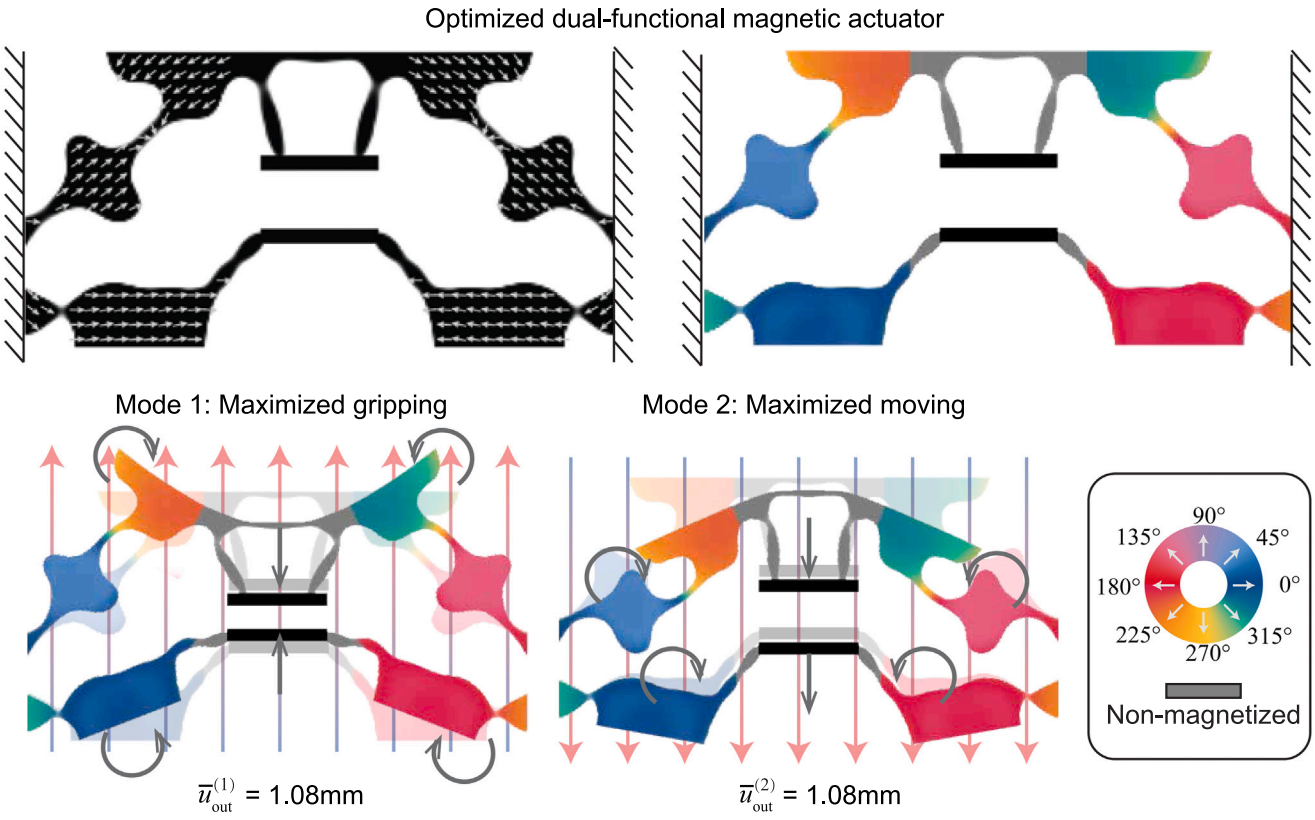


**Fig. 8.** Dual-functional magnetic actuators demonstrating the capability to grip and move objects under varied external magnetic fields. (For interpretation of the references to colour in this figure legend, the reader is referred to the web version of this article.)

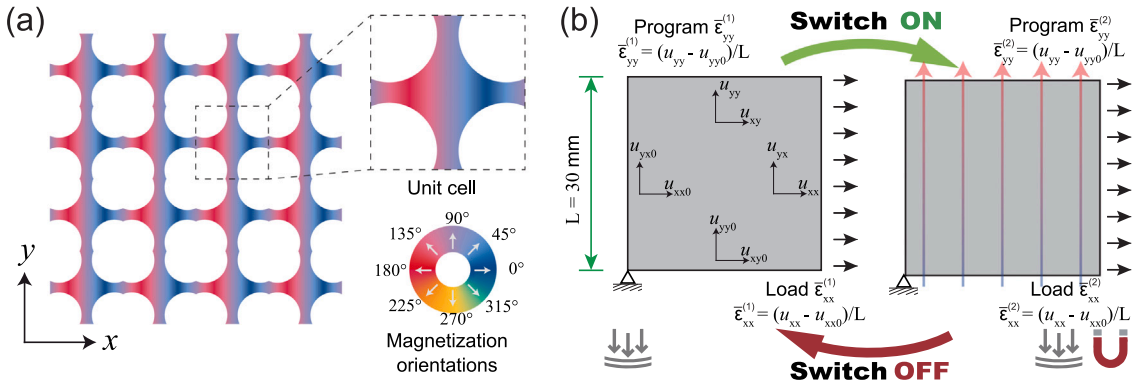


**Fig. 9.** Design setup of a magnetic metamaterial with programmable lateral deformation: (a) periodic metamaterial and unit cell; (b) purely mechanical and magento-mechanical load cases.

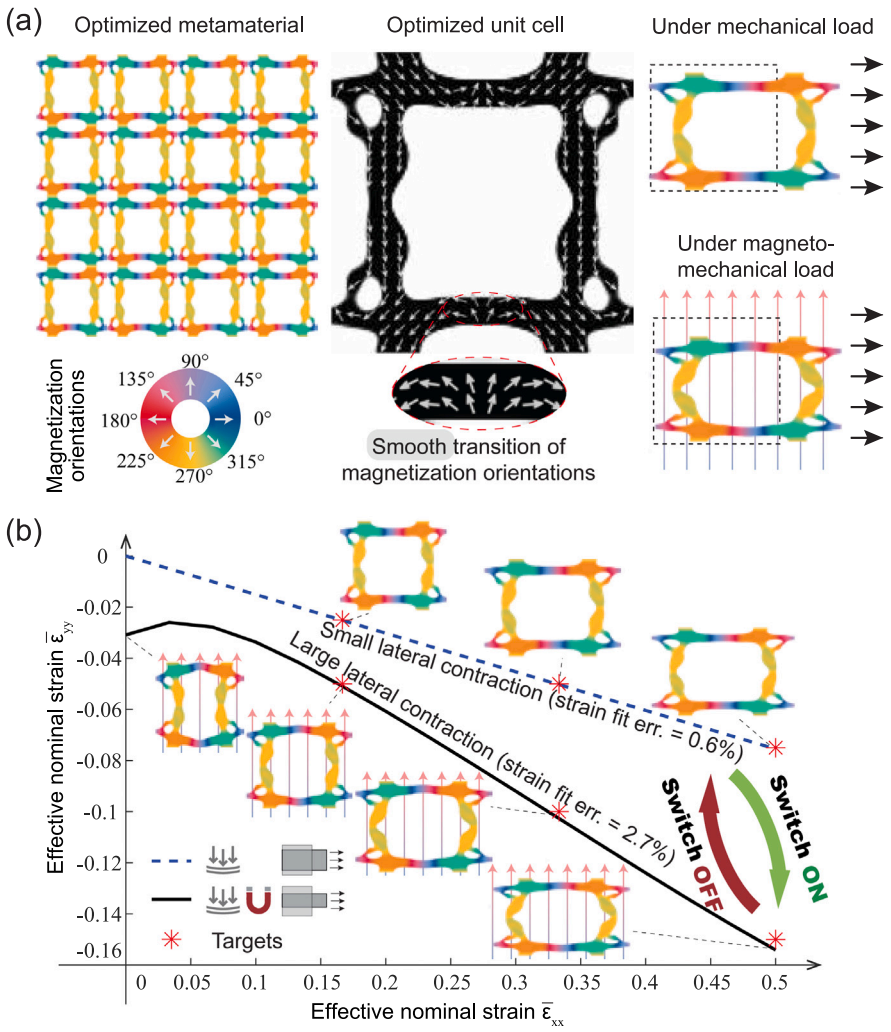


**Fig. 10.** Programming two levels of lateral contractions under purely mechanical and magneto-mechanical loads: (a) an optimized design and deformation configurations; (b) $\bar{\varepsilon}_{yy} - \bar{\varepsilon}_{xx}$ relations. (For interpretation of the references to colour in this figure legend, the reader is referred to the web version of this article.)

the strain distribution can be larger than 0.1, which necessitates the use of nonlinear finite deformation analysis in this study. Also, the $E_{xx}$ for the horizontal members are significantly larger than other members because they undergo horizontal mechanical stretching. Comparing the strain distributions under the two stimuli scenarios, we find the component $E_{yy}$ significantly differs from the other three components $E_{xx}$, $E_{yx}$, and $E_{xy}$. The vertical members (circled in Fig. 12) show tension strain in the $y$ direction due to magnetic actuation, leading to the programmed lateral expansion shown in Fig. 11.

In summary, the proposed optimization framework allows programmable control of complex magnetic metamaterials with continuous magnetization orientations, enabling the achievement of versatile behaviors.

## 4. Prototyping and experimental demonstration

We employ the direct ink writing (DIW) fabrication method, which has demonstrated effectiveness in the additive manufacturing of soft materials (Kim et al., 2018; Chen et al., 2024), to produce magnetized parts of optimized designs shown in Figs. 7 and 8 with continuous magnetization orientations. Notably, the DIW method is particularly effective for fabricating magnetic designs with continuous magnetization orientations, as it allows for a seamless printing path that can be aligned with the direction of magnetization. For the non-magnetized parts, the soft components are produced using the mold-casting method, while the nearly rigid components are fabricated using polylactic acid (PLA) through fused deposition modeling 3D printing. Different parts are bonded using adhesives. We experimentally demonstrate the performance of fabricated prototypes.

### 4.1. Direct-ink-writing fabrication

The ink material comprises a blend of PDMS, Ecoflex 00-30 Part B, fumed silica nanoparticles, and NdFeB magnetic particles with an average size of 5 μm (Kim et al., 2018). The material ingredients are thoroughly mixed using a planetary mixer. Subsequently, the ink material undergoes magnetization through an impulse magnetizer. For dispensing the magnetic ink material in a controllable manner, a customized gantry system and an air pressure-based dispenser are employed. A magnet is fixed to the nozzle to realign the magnetic particles within the liquid-state soft material, ensuring the magnetization direction aligns with the printing direction. A magnetic shielding is applied to prevent the influence of the magnet on the printed samples. The printing setup is shown in Fig. 13(a). It is crucial to note that the printing path, illustrated in Fig. 13(b), is determined based on the optimized design, aligning with the magnetization direction. The two fabricated prototypes are shown in Fig. 13(c). To accommodate the printing resolution, we scale up the design by three times and enlarge the thin connections in the dual-motion magnetic actuator design. To verify the printing quality, we measure the vertical member size of the printed magnetic gripper to be approximately 4 mm, compared to the target size of 3.8 mm.

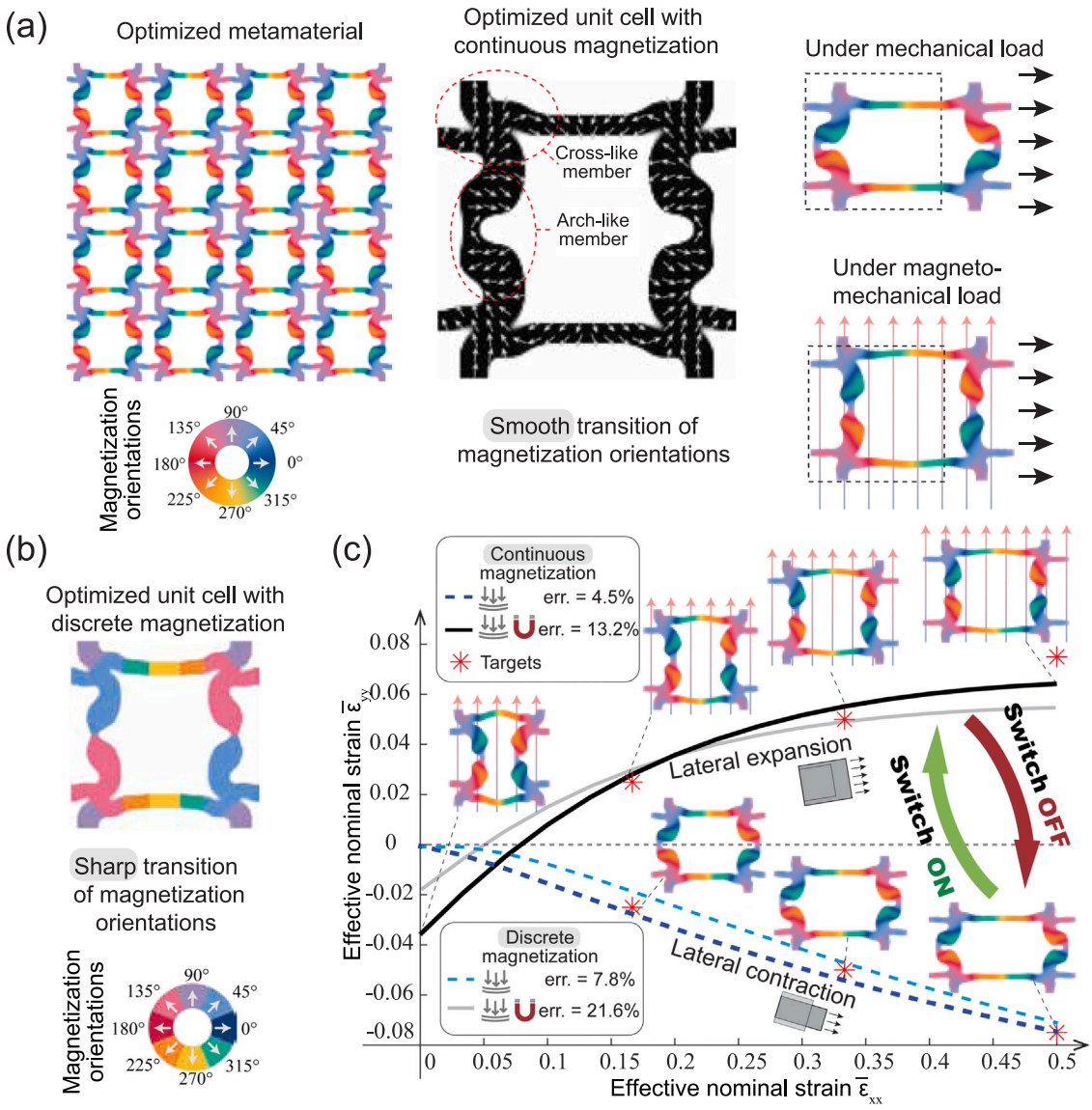


**Fig. 11.** Programming lateral contraction and expansion under purely mechanical and magneto-mechanical loads, respectively: (a) an optimized unit cell and deformation configurations with continuous magnetization; (b) an optimized unit cell with discrete magnetization; (c) $\bar{\varepsilon}_{yy} - \bar{\varepsilon}_{xx}$ relations.

The magnetization outcome in the fabricated samples is crucial for achieving the target magneto-mechanical responses. The magnetized area may have an influence on the magnetization distribution of adjacent regions, which we discuss in three aspects. First, during DIW fabrication, magnetized printed areas generate a small amount of magnetic field that could potentially affect adjacent regions. This effect is anticipated to be insignificant because of the small self-generated magnetic field and the presence of fumed silica in the ink material, which increases the viscosity and impedes the easy rotation of magnetic particles under a weak magnetic field. Second, for a fabricated sample, the self-generated magnetic field from magnetized regions could impact the magnetization field of adjacent areas due to non-zero magnetic susceptibility. Our magnetostatic simulation (Appendix C) indicates that this influence is small and possibly negligible. Third, the self-generated magnetic field could induce initial deformation, indirectly affecting the Eulerian magnetization field of adjacent regions. Although significant magneto-induced initial deformation is not observed in our fabricated design (see Fig. 13), we acknowledge that further investigation into magneto-mechanical self-interaction is necessary for future studies.

### 4.2. Experimental demonstration for magnetic actuator designs

We experimentally demonstrate the magneto-mechanical actuation performances of the discovered designs under external magnetic fields generated by a Helmholtz coil. The magnetic gripper actuation is shown in Fig. 14(a). We define the gripping ratio as the ratio of the magneto-actuated gripping distance of the nearly rigid components divided by the gap distance between the nearly rigid components without the magnetic field. Successful gripping performance is achieved with a gripping ratio of 76% under an upward magnetic field of 40 mT strength. Furthermore, we quantify the relationship between the gripping ratio and the applied external magnetic field in Fig. 14(b). As the magnetic field strength increases, the gripping ratio also increases.

In Fig. 15, we demonstrate the dual-functional magneto-mechanical performance of the fabricated magnetic actuator prototype. In addition to the gripping ratio, we define the performance metric, the moving ratio, as the average movement distance of the nearly rigid components under a magnetic field divided by the gap distance between the nearly rigid components without the magnetic field. Under upward and downward magnetic fields with 30 mT strength, we observe that the actuator can achieve the gripping and moving target performances with

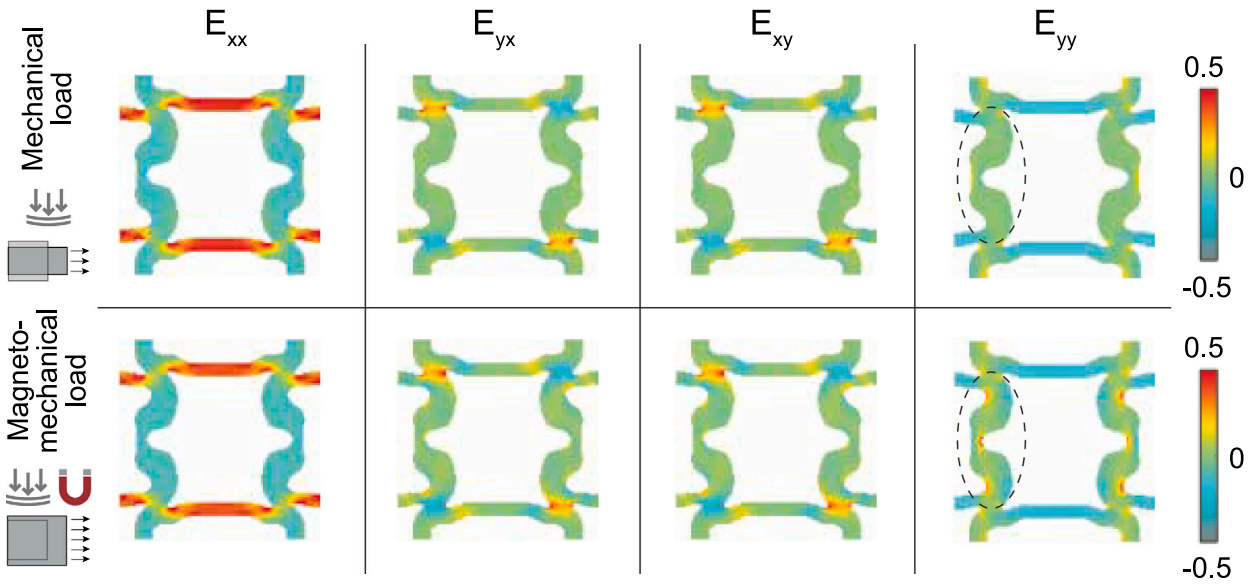


**Fig. 12.** Green–Lagrangian strain distributions for an optimized design (with programmed lateral contraction and expansion) under the applied engineering nominal strain of $\bar{\epsilon}_{xx} = 0.5$.

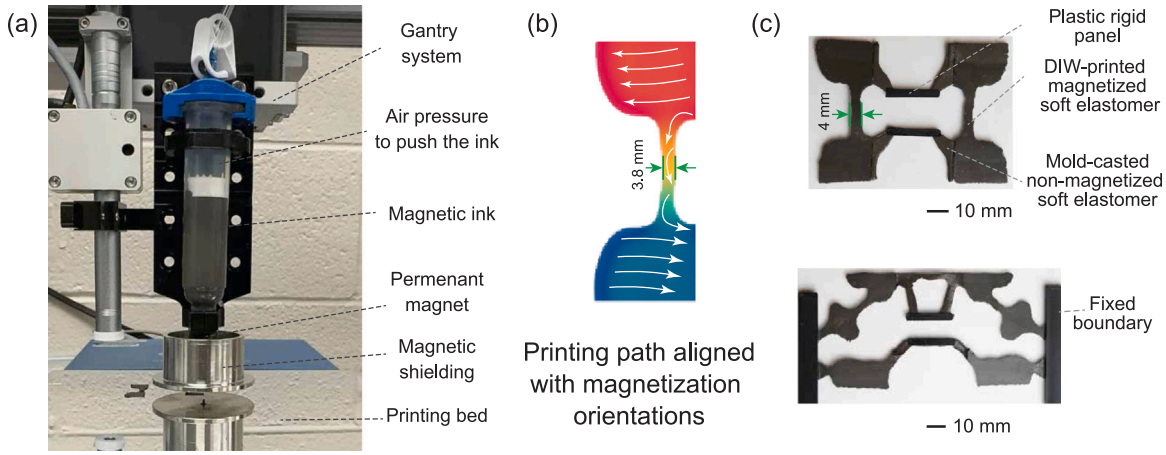


**Fig. 13.** Direct-ink-writing prototyping and experimental demonstration for an optimized design with continuous magnetization orientations: (a) printing setup; (b) printing path; (c) fabricated samples.

the designed deformation modes as shown in Fig. 8. The experimentally measured gripping and moving ratios are 58% and 103%, respectively. We acknowledge that the individual displacements of the two rigid components are not the same, which differs from the simulation results. This discrepancy may be caused by surface friction during actuation and inconsistent material property. We clarify that the focus of this study is on the theoretical and computational optimization framework, and the experimental results aim to provide a proof-of-concept demonstration. This demonstration does not contain a quantitative comparison between experimental and numerical results due to the need for accurate characterization of the printing material properties. More comprehensive material characterization, improved fabrication techniques, and extensive experimental investigations are planned for future work.

We measure the response time of the fabricated magnetic design to be 0.1–0.3 s, which is consistent with the values reported in the literature (Kim et al., 2018). In this study, we do not focus on controlling the response time; however, we note that the quick and controllable response time of hard-magnetic soft materials can be a significant benefit for biomedical applications.

## 5. Conclusion

To conclude, this paper introduces an innovative design framework for magnetic soft materials, with a parameterization scheme that optimizes continuous remanent magnetization orientations and material geometry. Through three illustrative examples, we demonstrate the effectiveness of this approach. Example 1 showcases the achievement of letter shapes using the optimization framework. Example 2 highlights the capability to design functional actuators by optimizing both continuous magnetization and geometry. In the final example, we create magneto-mechanical metamaterials capable of controlled lateral deformation under mechanical and magnetic stimuli. Notably, the examples underscore the advantages in performance and avoiding sharp changes in magnetization offered by our continuous magnetization parameterization over discrete methods. Additionally, we successfully use the direct-ink-writing approach to fabricate and demonstrate the performance of magnetic actuator designs with continuous remanent magnetization orientations.

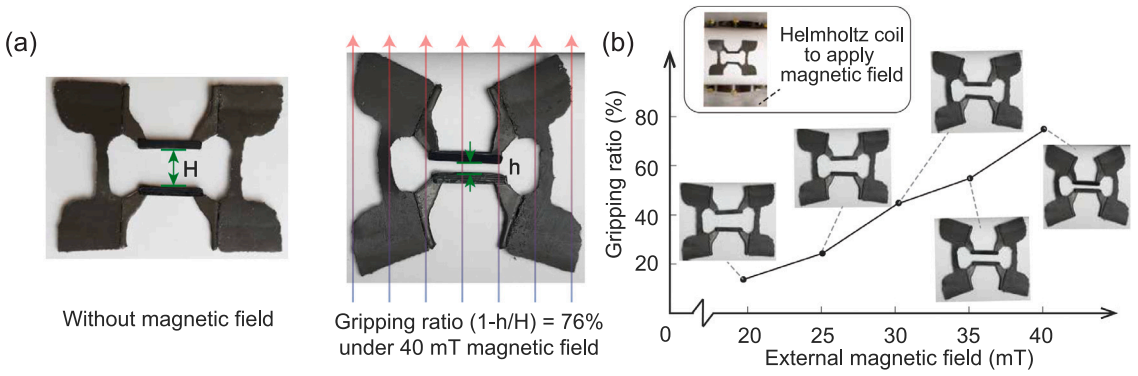


**Fig. 14.** Experimental demonstration of fabricated magnetic gripper: (a) gripping performance of the magnetic gripper; (b) relationship between gripping ratio and external magnetic field.

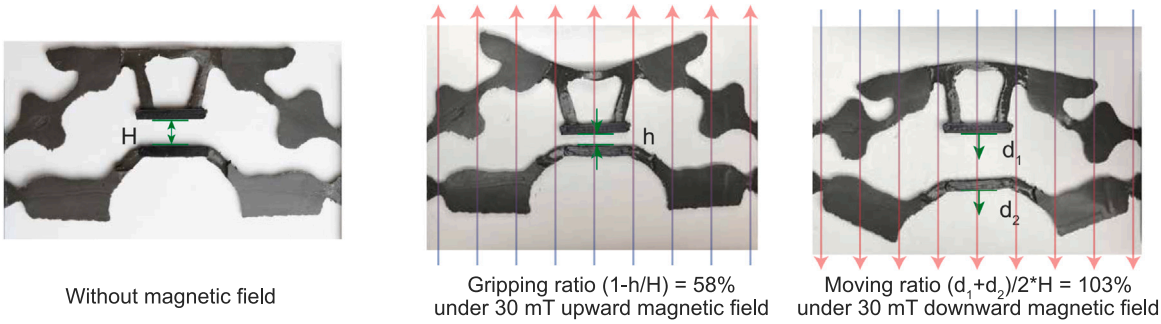


**Fig. 15.** Experimental demonstration of fabricated dual-functional magnetic actuator.

Extending our approach to three dimensions (3D) is an important future work, presenting both challenges and benefits. The computational burden increases due to more finite element degrees of freedom, which can be mitigated using advanced computational techniques such as those presented in the paper (Ferrari and Sigmund, 2020). Fabrication also poses a challenge, as our current magnetic direct-ink-writing technique primarily supports 2D magnetization, with true 3D magnetization orientations requiring further research. However, the 3D extension enlarges the design space and offers significant benefits, such as enhanced control over magnetic robots for complex motions, especially in biomedical applications, and the potential to design multi-functional 3D magnetic materials with increased versatility and improved performance.

Additionally, a more comprehensive characterization and experimental study for designs with continuous magnetization orientations is an important next step. Conducting numerical simulations that incorporate coupled magneto-mechanical interactions with the air domain (Moreno-Mateos et al., 2023; Rambausek and Schöberl, 2023) and the stretch-independent consideration of remanent magnetization (Danas and Reis, 2024; Yan et al., 2023; Moreno-Mateos et al., 2023) will be imperative to verify and understand the potential limitations of the simplified magnetic soft material model used for optimized designs with complex magnetization distributions in the current work.

## CRediT authorship contribution statement

**Zhi Zhao:** Writing – review & editing, Writing – original draft, Visualization, Software, Methodology, Investigation, Formal analysis. **Chao Wang:** Writing – review & editing, Writing – original draft, Validation, Investigation, Formal analysis, Data curation. **Xiaojia Shelly Zhang:** Writing – review & editing, Writing – original draft, Supervision, Resources, Project administration, Methodology, Investigation, Funding acquisition, Conceptualization.

## Declaration of competing interest

The authors declare that they have no known competing financial interests or personal relationships that could have appeared to influence the work reported in this paper.

## Data availability

Data will be made available on request.

## Acknowledgments

The authors acknowledge the financial support from the U.S. Defense Advanced Research Projects Agency (DARPA) Young Faculty Award (N660012314013) and the U.S. National Science Foundation (NSF) CAREER Award CMMI-2047692 and NSF Award CMMI-2245251. The information provided in this paper is the sole opinion of the authors and does not necessarily reflect the view of the sponsoring agency.

## Appendix A. Constitutive model and finite element analysis for hard-magnetic soft materials

This section provides a concise overview of the constitutive model that describes the magneto-mechanical behavior of magnetic soft materials under finite deformations. It is followed by a discussion of the corresponding finite element analysis, which employs a total Lagrangian framework.

Consider a deformable solid occupying a domain $\Omega$ in its undeformed state, where $\mathbf{X}$ represents the position vector. The solid is subjected to an applied displacement field $\bar{\mathbf{u}}$ on the boundary $\Gamma_u$ and an applied traction on $\Gamma_t$, such that $\Gamma_u \cup \Gamma_t = \partial\Omega$ and $\Gamma_u \cap \Gamma_t = \emptyset$. The deformation of the solid is described by a deformation map $\chi$, which maps a material point $\mathbf{X}$ to its corresponding position $\mathbf{x} = \chi(\mathbf{X})$. The

deformation gradient tensor $\mathbf{F}$ is defined as $\mathbf{F} = \nabla\chi$, where $\nabla$ denotes the gradient operator with respect to the undeformed configuration.

We employ a simplified model for ideal hard-magnetic soft materials developed in Zhao et al. (2019), which is described by the following Helmholtz free energy function (per unit volume in the undeformed configuration):

$$W(\mathbf{F}) = W_{\mathrm{E}}(\mathbf{F}) + W_{\mathrm{M}}(\mathbf{F}) = W_{\mathrm{E}}(\mathbf{F}) - \frac{1}{\mu_0}\mathbf{F}\mathbf{B}_{\mathrm{r}} \cdot \mathbf{B}_{\mathrm{a}}, \tag{16}$$

where $W_{\mathrm{M}}(\mathbf{F})$ is magnetic free energy; $W_{\mathrm{E}}(\mathbf{F})$ is the hyperelastic stored energy for soft matrix materials (e.g., elastomers) with magnetic particles. We note that this model relies on several important assumptions: a linear magnetic permeability identical to air or vacuum (zero magnetic susceptibility under small magnetic field after the material is fully magnetized), the neglect of dipole–dipole interaction, and the assumption of a uniform magnetic field. Despite its simplifications, the model shows good agreement with experimental results (Zhao et al., 2019) and can be solved with a relatively low computational burden, which is favorable for iterative topology optimization.

For the mechanical part, we utilize an isotropic and incompressible hyperelastic stored energy model of filled elastomers (Leonard et al., 2020). The model can be expressed as follows:

$$W_{\mathrm{E}}(\mathbf{F}) = (1-c)\psi\left(\tilde{I}_1\right) \quad \text{with} \quad \tilde{I}_1 = \frac{I_1 - 3}{(1-c)^{7/2}} + 3, \tag{17}$$

where $c$ represents the volume ratio for magnetic particles, and $I_1$ is the first principal invariant of the right Cauchy–Green deformation tensor $\mathbf{C} = \mathbf{F}^{\mathrm{T}}\mathbf{F}$. The function $\psi(\cdot)$ is defined by the expression given in (Lopez-Pamies, 2010):

$$\psi\left(\tilde{I}_1\right) = \sum_{i=1}^{N_{\mathrm{L}}} \frac{3^{1-\alpha_i}}{2\alpha_i}\mu_i\left(\tilde{I}_1^{\alpha_i} - 3^{\alpha_i}\right) \tag{18}$$

where $\alpha_i$ $(i = 1, 2, \ldots, N_{\mathrm{L}})$ are real-valued constants and $\mu = \sum_{i=1}^{N_{\mathrm{L}}}\mu_i$ is the second Lamé parameter under the initial state. In this study, we consider two sets of terms in the hyperelastic stored energy function, i.e., $N_{\mathrm{L}} = 2$. In the numerical examples in Section 3, we utilize two sets of characterized material parameters corresponding to PDMS with a base-to-agent ratio of 20 to 1 (Example 2) and Ecoflex 00-30 (Examples 1 and 3) containing magnetic particles at a volume ratio of 15% (c = 0.15). For the 20 : 1 base-to-agent PDMS, the material constants are: $\alpha_1 = 1.4234$, $\alpha_2 = 0.5001$, $\mu_1 = 0.0989$ MPa, and $\mu_2 = 0.0882$ MPa. For the Ecoflex 00-30 material, the material constants are: $\alpha_1 = 0.9001$, $\alpha_2 = 1.2218$, $\mu_1 = 0.0145$ MPa, and $\mu_2 = 0.0144$ MPa.

In the undeformed configuration, the equilibrium of the solid is governed by the following partial differential equations with body force neglected:

$$\begin{aligned} &\nabla\cdot\mathbf{P} = \mathbf{0} \quad \text{in} \quad \Omega, \\ &\mathbf{u} = \tilde{\mathbf{u}} \quad \text{on} \quad \Gamma_{\mathrm{u}}, \\ &\mathbf{P}\mathbf{N} = \tilde{\mathbf{t}} \quad \text{on} \quad \Gamma_{\mathrm{t}}, \end{aligned} \tag{19}$$

where $\mathbf{P}$ is the first Piola–Kirchhoff stress, $\nabla\cdot$ stands for the divergence operator in the undeformed configuration, $\mathbf{N}$ is the outward unit vector normal to the undeformed boundary of the solid, and $\tilde{\mathbf{t}}$ is the applied traction.

Based on finite element theory (Belytschko et al., 2014), we construct a finite element mesh $\Omega_{\mathrm{h}}$ consisting of $N_{\mathrm{e}}$ elements and $N_{\mathrm{n}}$ nodes. We can express the total potential energy $\Pi(\mathbf{u})$ and its stationary condition $\mathbf{r}(\mathbf{u})$ as follows:

$$\Pi(\mathbf{u}) = \sum_{e=1}^{N_{\mathrm{e}}}\int_{\Omega_e} W\left(\mathbf{u}_e\right)\mathrm{d}\mathbf{X} - \left(\mathbf{f}_{\mathrm{ext}}\right)^{\mathrm{T}}\mathbf{u}, \tag{20}$$

and

$$\mathbf{r}(\mathbf{u}) = \frac{\partial\Pi}{\partial\mathbf{u}}(\mathbf{u}) = \mathbf{f}_{\mathrm{int}}(\mathbf{u}) - \mathbf{f}_{\mathrm{ext}} = \mathbf{0}, \tag{21}$$

respectively, where $\Omega_e$ is the elementwise mesh domain, $\mathbf{u}$ represents the displacement vector, $\mathbf{r}$ is the global residual vector, $\mathbf{f}_{\mathrm{int}}$ is the internal force vector, and $\mathbf{f}_{\mathrm{ext}}$ is the external force vector. To solve the nonlinear system of equations, the Newton–Raphson procedure with an inexact line search method (Armijo, 1966; Zhang et al., 2017) is used iteratively. This study employs displacement-based finite elements in 2D under the plane stress condition, which ensures that volumetric locking does not occur even for soft materials with incompressible behaviors.

## Appendix B. Parameterization of discrete magnetization distribution using hypercube-to-simplex projection

The residual magnetic flux density in each location of the design is chosen from a predetermined set of $N_{\mathrm{m}}$ candidate residual magnetic flux densities, denoted as $\mathbf{B}_{\mathrm{r}}^{(1)}, \ldots, \mathbf{B}_{\mathrm{r}}^{(N_{\mathrm{m}})}$, each pointing in a specific direction. The residual magnetic flux density in element $e$ is expressed as:

$$\mathbf{B}_{\mathrm{r},e} = \sum_{j=1}^{N_{\mathrm{m}}}\left(\overline{m}_e^{(j)}\right)^{p_m}\mathbf{B}_{\mathrm{r}}^{(j)}. \tag{22}$$

In the above interpolation, $\overline{m}_e^{(j)}$ represents the physical magnetization variable which indicates the magnetization of element $e$: $\overline{m}_e^{(j)} = 1$ means that the $j$th candidate residual magnetic flux density $\mathbf{B}_{\mathrm{r}}^{(j)}$ is selected, while $\overline{m}_e^{(j)} = 0$ indicates that the $j$th candidate residual magnetic flux density $\mathbf{B}_{\mathrm{r}}^{(j)}$ is not selected. To penalize the mixture of candidate magnetizations, we introduce a SIMP-type (Bendsøe, 1989; Bendsoe and Sigmund, 2003) penalization power $p_m$.

To further promote discrete magnetization distribution and accommodate non-magnetized regions in our designs, we adopt the Hypercube-to-Simplex Projection (HSP) approach (Zhou et al., 2018). The HSP approach has demonstrated robust performance based on our prior experience (Zhao and Zhang, 2022), and its expression is provided below:

$$\overline{m}_e^{(j)} = \sum_{i=1}^{2^{N_{\mathrm{m}}}} s_i^{(j)}\left((-1)^{\left(N_{\mathrm{m}}+\sum_{k=1}^{N_{\mathrm{m}}}c_i^{(k)}\right)}\prod_{k=1}^{N_{\mathrm{m}}}\left(\overline{\xi}_e^{(k)} + c_i^{(k)} - 1\right)\right), \tag{23}$$

where $\overline{\xi}_e^{(j)}$ is the intermediate variable obtained from similar filtering and projection operations. The parameter $c_i^{(j)} = \{0, 1\}$ is the $i$th vertex of a $N_{\mathrm{m}}$-dimensional unit hypercube for the $j$th candidate remanent magnetization vector, and $s_i^{(j)}$ is the mapped vertex of a $N_{\mathrm{m}}$-dimensional standard simplex domain:

$$s_i^{(j)} = \begin{cases} \dfrac{c_i^{(j)}}{\sum_{k=1}^{N_{\mathrm{m}}}c_i^{(k)}} & \text{if } \sum_{k=1}^{N_{\mathrm{m}}}c_i^{(k)} \geq 1, \\ 0 & \text{otherwise.} \end{cases} \tag{24}$$

## Appendix C. Impact of non-zero magnetic susceptibility on magnetization distribution

In this appendix, we investigate the impact of magnetized areas on their adjacent regions due to non-zero magnetic susceptibility. We conduct a magnetostatic simulation to obtain the magnetization field for an optimized magnetic design with continuous remanent magnetization.

Consider a hard-magnetic material with remanent magnetization $\mathbf{M}_{\mathrm{r}} = \frac{1}{\mu_0}\mathbf{B}_{\mathrm{r}}$ and permeability $\mu = (1 + \chi_{\mathrm{v}})\mu_0$ embedded in a large air domain with permeability $\mu_0$. We aim to determine the magnetization distribution $\mathbf{M}$ and compare it with remanent magnetization distribution $\mathbf{M}_{\mathrm{r}}$. In magnetostatics without free electric current, Maxwell's equations are presented as:

$$\nabla\times\mathbf{H} = 0 \tag{25}$$

$$\nabla\cdot\mathbf{B} = 0, \tag{26}$$

where $\mathbf{H}$ is magnetic field strength, and $\mathbf{B}$ is magnetic flux density. The constitutive relations for magnetic fields are given by:

$$\mathbf{B} = \mu\mathbf{H} + \mu_0\mathbf{M}_{\mathrm{r}}. \tag{27}$$

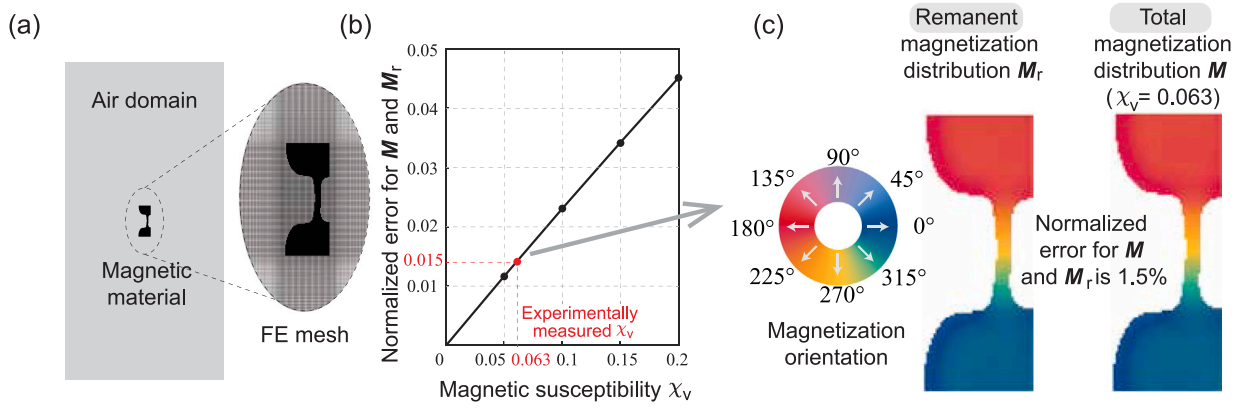


**Fig. 16.** Magnetostatic simulation for a pre-magnetized hard-magnetic material with continuous remanent magnetization: (a) problem setup and finite element mesh; (b) normalized error for total magnetization **M** and remanent magnetization $r$ with increasing magnetic susceptibility $\chi_v$; (c) comparison of magnetization distributions when $\chi_v = 0.063$.

Assuming the magnetic field strength is derived from a scalar potential $\phi$, we have:

$$\mathbf{H} = -\nabla\phi. \tag{28}$$

The Ampère's law can be automatically satisfied. Substituting into Gauss's law for magnetism, we obtain:

$$-\nabla\cdot(\mu\nabla\phi) = -\nabla\cdot(\mu_0\mathbf{M}_r). \tag{29}$$

To solve the above equation, we use the finite element method. The weak form of the equation is used for numerical computation. As shown in Fig. 16(a), the domain is discretized into structured quadrilateral elements, with a finer mesh for the magnetic material and a coarser mesh for the air domain to save computational time while ensuring good accuracy. We set the magnetic scalar potential $\phi$ zero on the air domain boundaries to approximate the far-field behavior. We experimentally measure a direct-ink-writing fabricated sample using a vibrating sample magnetometer. The measured remanent magnetization, $\mathbf{M}_r$, is 33.2 kA/m and initial magnetic susceptibility, $\chi_v$, is 0.063. We solve for the boundary value problem and obtain the magnetization field using the following relation

$$\mathbf{M} = \chi_v(-\nabla\phi) + \mathbf{M}_r. \tag{30}$$

We use the following normalized error metric to compare two vector fields:

$$\text{Normalized err.} = \frac{\|\mathbf{M}-\mathbf{M}_r\|_2}{\|\mathbf{M}_r\|_2} \tag{31}$$

We take the left part of the magnetic design shown in Fig. 7(b) as an example for investigation. We vary the magnetic susceptibility $\chi_v$ within the range of 0.01 to 0.2, typically applicable for hard-magnetic materials (see Danas and Reis (2024)). In Fig. 16(b), the normalized error increases with the rising of $\chi_v$, but remains small (<0.1). We plot the magnetization orientation distributions in Fig. 16(c) with our experimentally measured data $\chi_v = 0.063$, and observe that the magnetization orientation is almost the same and the normalized error is 0.3. Based on the magnetization simulation results in this appendix, we conclude that the impact of magnetized areas on their adjacent regions due to non-zero magnetic susceptibility is small and can be assumed to be negligible. This assumption is often used in modeling for hard-magnetic soft materials (Zhao et al., 2019; Yan et al., 2023; Moreno-Mateos et al., 2023).

## References


Armijo, L., 1966. Minimization of functions having Lipschitz continuous first partial derivatives. Pacific J. Math. 16 (1), 1–3.

Belytschko, T., Liu, W.K., Moran, B., Elkhodary, K., 2014. Nonlinear Finite Elements for Continua and Structures. John wiley & sons.

Bendsøe, M.P., 1989. Optimal shape design as a material distribution problem. Struct. Optim. 1 (4), 193–202.

Bendsoe, M.P., Sigmund, O., 2003. Topology Optimization: Theory, Methods, and Applications. Springer Science & Business Media.

Bourdin, B., 2001. Filters in topology optimization. Internat. J. Numer. Methods Engrg. 50 (9), 2143–2158.

Bruggi, M., 2008. On an alternative approach to stress constraints relaxation in topology optimization. Struct. Multidiscip. Optim. 36 (2), 125–141.

Ceylan, H., Yasa, I.C., Yasa, O., Tabak, A.F., Giltinan, J., Sitti, M., 2019. 3D-printed biodegradable microswimmer for theranostic cargo delivery and release. ACS Nano 13 (3), 3353–3362.

Chen, T., Pauly, M., Reis, P.M., 2021. A reprogrammable mechanical metamaterial with stable memory. Nature 589 (7842), 386–390.

Chen, W., Wang, R., Liu, K., 2024. Active compliant mechanisms for optimized actuation by LCE-based artificial muscles. Mech. Mater. 189, 104879.

Danas, K., Reis, P.M., 2024. Stretch-independent magnetization in incompressible isotropic hard magnetorheological elastomers. J. Mech. Phys. Solids 191, 105764.

Duysinx, P., Bendsøe, M.P., 1998. Topology optimization of continuum structures with local stress constraints. Internat. J. Numer. Methods Engrg. 43 (8), 1453–1478.

Ferrari, F., Sigmund, O., 2020. A new generation 99 line Matlab code for compliance topology optimization and its extension to 3D. Struct. Multidiscip. Optim. 62, 2211–2228.

Kang, S.S., Choi, K., Nam, J.-D., Choi, H.J., 2020. Magnetorheological elastomers: Fabrication, characteristics, and applications. Materials 13 (20), 4597.

Kim, Y., Parada, G.A., Liu, S., Zhao, X., 2019. Ferromagnetic soft continuum robots. Science Robotics 4 (33).

Kim, Y., Yuk, H., Zhao, R., Chester, S.A., Zhao, X., 2018. Printing ferromagnetic domains for untethered fast-transforming soft materials. Nature 558 (7709), 274–279.

Leonard, M., Wang, N., Lopez-Pamies, O., Nakamura, T., 2020. The nonlinear elastic response of filled elastomers: Experiments vs. theory for the basic case of particulate fillers of micrometer size. J. Mech. Phys. Solids 135, 103781.

Li, Y., Li, J., Li, W., Du, H., 2014. A state-of-the-art review on magnetorheological elastomer devices. Smart Mater. Struct. 23 (12), 123001.

Lloyd, P., Hoshiar, A.K., da Veiga, T., Attanasio, A., Marahrens, N., Chandler, J.H., Valdastri, P., 2020. A learnt approach for the design of magnetically actuated shape forming soft tentacle robots. IEEE Robot. Autom. Lett. 5 (3), 3937–3944.

Lopez-Pamies, O., 2010. A new I1-based hyperelastic model for rubber elastic materials. C. R. Mec. 338 (1), 3–11.

Lu, L., Sim, J., Zhao, R.R., 2023. Mechanics of hard-magnetic soft materials: A review. Mech. Mater. 104874.

Lum, G.Z., Ye, Z., Dong, X., Marvi, H., Erin, O., Hu, W., Sitti, M., 2016. Shape-programmable magnetic soft matter. Proc. Natl. Acad. Sci. 113 (41), E6007–E6015.

Ma, C., Chang, Y., Wu, S., Zhao, R.R., 2022. Deep learning-accelerated designs of tunable magneto-mechanical metamaterials. ACS Appl. Mater. Interfaces 14 (29), 33892–33902.

Moreno-Mateos, M.A., Danas, K., Garcia-Gonzalez, D., 2023. Influence of magnetic boundary conditions on the quantitative modelling of magnetorheological elastomers. Mech. Mater. 184, 104742.

Nemat-Nasser, S., Hori, M., 2013. Micromechanics: Overall Properties of Heterogeneous Materials. Elsevier.

Nomura, T., Dede, E.M., Lee, J., Yamasaki, S., Matsumori, T., Kawamoto, A., Kikuchi, N., 2015. General topology optimization method with continuous and discrete orientation design using isoparametric projection. Internat. J. Numer. Methods Engrg. 101 (8), 571–605.

Olhoff, N., 1989. Multicriterion structural optimization via bound formulation and mathematical programming. Struct. Optim. 1 (1), 11–17.
Rahmati, A.H., Jia, R., Tan, K., Liu, L., Zhao, X., Deng, Q., Sharma, P., 2023a. Giant magnetoelectricity in soft materials using hard magnetic soft materials. Mater. Today Phys. 100969.
Rahmati, A.H., Jia, R., Tan, K., Zhao, X., Deng, Q., Liu, L., Sharma, P., 2023b. Theory of hard magnetic soft materials to create magnetoelectricity. J. Mech. Phys. Solids 171, 105136.
Rambausek, M., Schöberl, J., 2023. Curing spurious magneto-mechanical coupling in soft non-magnetic materials. Internat. J. Numer. Methods Engrg. 124, 2261–2291.
Svanberg, K., 1987. The method of moving asymptotes—a new method for structural optimization. Internat. J. Numer. Methods Engrg. 24 (2), 359–373.
Tian, J., Li, M., Han, Z., Chen, Y., Gu, X.D., Ge, Q., Chen, S., 2022. Conformal topology optimization of multi-material ferromagnetic soft active structures using an extended level set method. Comput. Methods Appl. Mech. Engrg. 389, 114394.
Wang, F., Lazarov, B.S., Sigmund, O., 2011. On projection methods, convergence and robust formulations in topology optimization. Struct. Multidiscip. Optim. 43 (6), 767–784.
Wang, F., Lazarov, B.S., Sigmund, O., Jensen, J.S., 2014a. Interpolation scheme for fictitious domain techniques and topology optimization of finite strain elastic problems. Comput. Methods Appl. Mech. Engrg. 276, 453–472.
Wang, F., Sigmund, O., Jensen, J.S., 2014b. Design of materials with prescribed nonlinear properties. J. Mech. Phys. Solids 69, 156–174.
Wang, C., Zhao, Z., Zhang, X.S., 2023. Inverse design of magneto-active metasurfaces and robots: Theory, computation, and experimental validation. Comput. Methods Appl. Mech. Engrg. 413, 116065.
Wu, S., Hamel, C.M., Ze, Q., Yang, F., Qi, H.J., Zhao, R., 2020. Evolutionary algorithm-guided voxel-encoding printing of functional hard-magnetic soft active materials. Adv. Intell. Syst. 2 (8), 2000060.
Yan, D., Aymon, B.F., Reis, P.M., 2023. A reduced-order, rotation-based model for thin hard-magnetic plates. J. Mech. Phys. Solids 170, 105095.
Zhang, X., Ramos, A.S., Paulino, G.H., 2017. Material nonlinear topology optimization using the ground structure method with a discrete filtering scheme. Struct. Multidiscip. Optim. 55 (6), 2045–2072.
Zhao, R., Kim, Y., Chester, S.A., Sharma, P., Zhao, X., 2019. Mechanics of hard-magnetic soft materials. J. Mech. Phys. Solids 124, 244–263.
Zhao, Z., Wang, C., Zhang, X.S., 2023. Tuning buckling behaviors in magnetically active structures: topology optimization and experimental validation. J. Appl. Mech. 90 (9).
Zhao, Z., Zhang, X.S., 2022. Topology optimization of hard-magnetic soft materials. J. Mech. Phys. Solids 158, 104628.
Zhao, Z., Zhang, X.S., 2023. Encoding reprogrammable properties into magneto-mechanical materials via topology optimization. npj Comput. Mater. 9 (1), 57.
Zhou, Y., Nomura, T., Saitou, K., 2018. Multi-component topology and material orientation design of composite structures (MTO-C). Comput. Methods Appl. Mech. Engrg. 342, 438–457.
Zhou, C., Yang, Y., Wang, J., Wu, Q., Gu, Z., Zhou, Y., Liu, X., Yang, Y., Tang, H., Ling, Q., et al., 2021. Ferromagnetic soft catheter robots for minimally invasive bioprinting. Nature Commun. 12 (1), 5072.